2nd Advanced Optical Metrology Compendium

Advanced Optical Metrology

Geoscience | Corrosion | Particles | Additive Manufacturing: Metallurgy, Cut Analysis & Porosity

EVIDENT OLYMPUS

WILEY

The latest eBook from Advanced Optical Metrology. Download for free.

This compendium includes a collection of optical metrology papers, a repository of teaching materials, and instructions on how to publish scientific achievements.

With the aim of improving communication between fundamental research and industrial applications in the field of optical metrology we have collected and organized existing information and made it more accessible and useful for researchers and practitioners.

EVIDENT OLYMPUS

WILEY

Check for updates

NANO · MICRO
small
www.small-journal.com

Simultaneous Dimensional and Analytical Characterization of Ordered Nanostructures

Philipp Hönicke, Yves Kayser, Konstantin V. Nikolaev, Victor Soltwisch, Jeroen E. Scheerder, Claudia Fleischmann, Thomas Siefke, Anna Andrle, Grzegorz Gwalt, Frank Siewert, Jeffrey Davis, Martin Huth, Anabela Veloso, Roger Loo, Dieter Skroblin, Michael Steinert, Andreas Undisz, Markus Rettenmayr, and Burkhard Beckhoff*

The spatial and compositional complexity of 3D structures employed in today's nanotechnologies has developed to a level at which the requirements for process development and control can no longer fully be met by existing metrology techniques. For instance, buried parts in stratified nanostructures, which are often crucial for device functionality, can only be probed in a destructive manner in few locations as many existing nondestructive techniques only probe the objects surfaces. Here, it is demonstrated that grazing exit X-ray fluorescence can simultaneously characterize an ensemble of regularly ordered nanostructures simultaneously with respect to their dimensional properties and their elemental composition. This technique is nondestructive and compatible to typically sized test fields, allowing the same array of structures to be studied by other techniques. For crucial parameters, the technique provides sub-nm discrimination capabilities and it does not require access-limited large-scale research facilities as it is compatible to laboratory-scale instrumentation.

1. Introduction

The amazing developments in the field of nanotechnology, especially the ever-decreasing feature dimensions and the more and more complex 3D nanostructures in semiconductor fabrication, boost the developments in many fields of today's scientific, industrial and everyday life. Examples include sensing applications,[1,2] metamaterials,[3] energy harvesting,[2,4,5] or other emerging applications.[2,4,6–10] Of course nanoelectronics is the most prominent example and the ongoing pursuit of Moore's law[11] results in a drastically increased complexity of the 3D structure of devices. Many different materials[12] are incorporated into devices with ever decreasing critical feature dimensions.[13–15] In addition, the growing importance of the third dimension for a further densification of the structures[16–18] makes it easy to imagine that these developments require a vastly increasing amount and new solutions of metrology in order to be producible at reasonable yields.[13,19–21] Both for the semiconductor related nanostructures and most of the other application fields, a key challenge to enable successful fabrication and application is related to the 3D and compositional characterization of such nanostructures[21–25] with sufficient discrimination capability, precision, and accuracy.

P. Hönicke, Y. Kayser, V. Soltwisch, A. Andrle, D. Skroblin, B. Beckhoff
Div. 7 - Temperature and Synchrotron Radiation
Physikalisch-Technische Bundesanstalt (PTB)
Abbestr. 2-12, 10587 Berlin, Germany
E-mail: philipp.hoenicke@ptb.de

K. V. Nikolaev
NRC Kurchatov Institute
pl. Akademika Kurchatova 1, Moscow 123182, Russia

J. E. Scheerder, C. Fleischmann, A. Veloso, R. Loo
imec
Kapeldreef 75, Leuven 3001, Belgium

C. Fleischmann
Quantum Solid-State Physics
KU Leuven, Celestijnenlaan 200D, Leuven 3001, Belgium

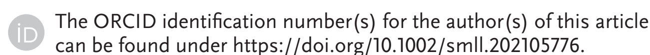
The ORCID identification number(s) for the author(s) of this article can be found under https://doi.org/10.1002/smll.202105776.

© 2021 The Authors. Small published by Wiley-VCH GmbH. This is an open access article under the terms of the Creative Commons Attribution-NonCommercial License, which permits use, distribution and reproduction in any medium, provided the original work is properly cited and is not used for commercial purposes.

DOI: 10.1002/smll.202105776

T. Siefke, M. Steinert
Abbe Center of Photonics
Friedrich Schiller University Jena
Max-Wien-Platz 1, 07745 Jena, Germany

G. Gwalt, F. Siewert
Helmholtz Zentrum Berlin für Materialien und Energie (HZB)
Albert-Einstein-Str. 15, 12489 Berlin, Germany

J. Davis
EOS GmbH
Robert-Stirling-Ring 1, 82152 Krailling, Germany

M. Huth
PNDetector GmbH
Otto-Hahn-Ring 6, 81739 München, Germany

A. Undisz
Technische Universität Chemnitz
Inst. für Werkstoffwiss. und Werkstofftech.
Erfenschlager Straße 73, 09125 Chemnitz, Germany

M. Rettenmayr
Otto Schott Institute of Materials Research
Friedrich Schiller University Jena
Löbdergraben 32, 07743 Jena, Germany

16136829, 2022, 6, Downloaded from https://onlinelibrary.wiley.com/doi/10.1002/smll.202105776 by EVIDENCE AID - BELGIUM, Wiley Online Library on [17/01/2023]. See the Terms and Conditions (https://onlinelibrary.wiley.com/terms-and-conditions) on Wiley Online Library for rules of use; OA articles are governed by the applicable Creative Commons License

The main metrology techniques available in this context are the electron microscopy-based techniques such as scanning electron microscopy (SEM) or transmission electron microscopy (TEM) but also atomic force microscopy (AFM) as well as photon-based techniques such as optical critical dimension (OCD) and small-angle X-ray scattering (CD-SAXS), grazing incidence SAXS and optical scatterometry. But, these techniques are either beginning to approach physical limitations, do not provide elemental sensitivity or do not have sufficient discrimination capability to some of the needed parameters.[22,23] For gate-all-around (GAA) devices for instance, the buried channel structure is no longer visible to an SEM but is crucial for device functionality.[26] Other existing techniques which can probe such buried structures require rather costly dedicated sample characteristics (e.g., mm-sized test fields due to large footprint in grazing incidence SAXS) or pretreatments (e.g., thinning of the whole wafer in transmission SAXS, lamella preparation in TEM or nontrivial tip preparation in atom probe tomography[27]). In addition, especially TEM and atom probe tomography (APT) can only investigate single or few objects, but often statistically representative data is needed. Consequently, there is a clear need for new metrology techniques to overcome the limitations of the existing metrology toolset.[22,23]

In this work, we demonstrate scanning-free grazing exit X-ray fluorescence (SF-GEXRF,[28] see **Figure 1**) as a new metrology technique in this highly relevant context and discuss its capabilities for characterizing 2D and 3D nanostructures with respect to their dimensional and compositional properties with sub-nm sensitivities. Even though the GEXRF technique itself is not new, its application to such nanostructures is and it has some highly promising features especially for application in the field of semiconductors: As X-ray fluorescence is element specific, analytic, or compositional information is provided if an energy-dispersive detector is used and due to the interaction of the X-ray fluorescence photons from within the nanostructures, one gains dimensional information for key parameters, for example, line heights or widths. Due to the rather high penetration depths of X-rays, also buried features of a nanostructure can be characterized to some extent without a necessity for cross sectioning or other destructive steps. In contrast to grazing incidence techniques, it does not require grazing excitation conditions and thus does not suffer from the large beam footprint on the sample surface. This reduces the required minimum area of identical nanostructures from several mm^2 to area sizes in the order of 100 µm by 100 µm or even smaller and enables the application to typical industrial test-field sizes.

Furthermore, SF-GEXRF probes many nanostructures at once providing ensemble information rather than probing only single or few selected nanostructures. As no sample preparation is required and the technique is non-destructive, it would also allow for subsequent application of other techniques such as TEM or APT for validation purposes. Other important requirements in this context, such as being automatable or having a reasonable throughput can certainly be addressed by further developments.

We are showing how the recently established reconstruction capabilities for 2D and 3D nanostructures employing grazing incidence XRF (GIXRF)[29–31] can be readily transferred to GEXRF measurements such that the dimensions and composition of a nanostructure can be reconstructed from the experimental data. The reconstruction relies on a finite-element based solver of the Maxwell equations[32] or many-beam dynamical diffraction theory (MB-DDT)[30] as well as an machine learning based highly efficient Bayesian optimizer (BO).[33,51] We also

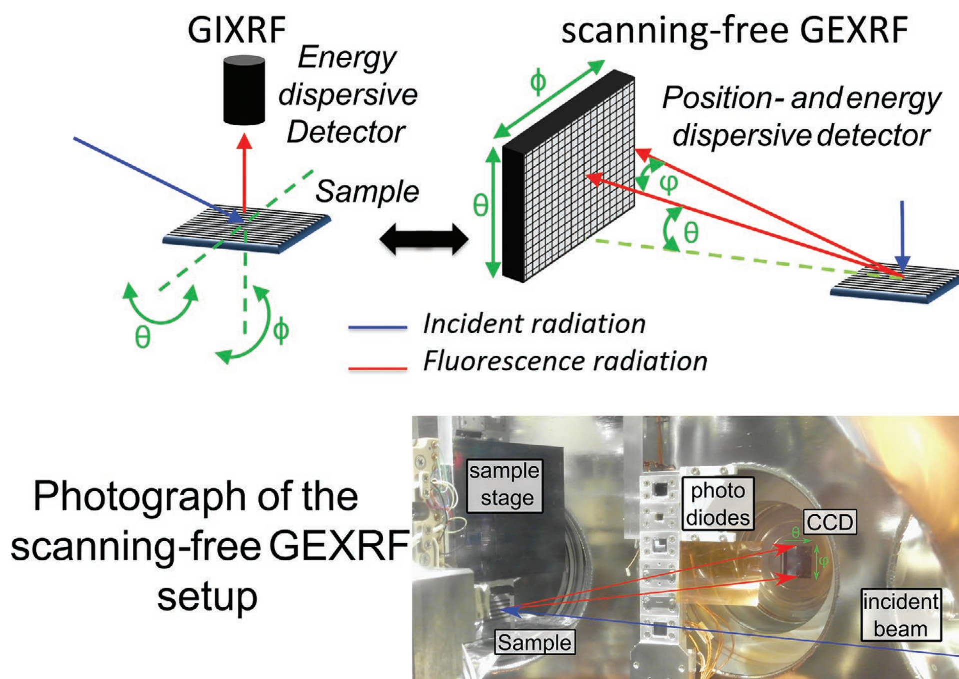

Figure 1. Schematic comparison of the basic geometry for GIXRF (grazing incidence X-ray fluorescence) and SF-GEXRF. The lower part shows an actual photograph of the setup employed in this work.

 © 2021 The Authors. Small published by Wiley-VCH GmbH

16136829, 2022, 6, Downloaded from https://onlinelibrary.wiley.com/doi/10.1002/smll.202105776 by EVIDENCE AID - BELGIUM, Wiley Online Library on [17/01/2023]. See the Terms and Conditions (https://onlinelibrary.wiley.com/terms-and-conditions) on Wiley Online Library for rules of use; OA articles are governed by the applicable Creative Commons License

compare the results to TEM and AFM data for validation. Furthermore, it is shown that such GEXRF characterizations can be performed employing relatively simple setups using commercial X-ray tubes rather than large-scale synchrotron facilities for excitation. Thus the methodology is expected to be much more accessible than other emerging characterization techniques for such nanostructure characterization.[34–36]

2. Results and Discussion

The basic principle of the technique is the interplay of the X-ray standing wave (XSW), which arises from an interference of fluorescence photons traveling on different paths inside the nanostructure toward the detector. Similarly to GIXRF, the intensity distribution inside the XSW is strongly dependent on the incident (grazing incidence geometry) or exit angles (grazing exit geometry) and serves as the nanoscale sensor. For regular arrays of nanostructures, the angle between the X-ray beam and the sample surface (θ) as well as the angle between the X-ray beam and the symmetry axis of the nanostructures pointing toward the detector (φ) are of interest (as depicted in Figure 1). Once the GEXRF experimental data is recorded, one can follow two directions to derive the required information about the nanostructure. As shown in **Figure 2**a), one can proceed with reconstructing the data by performing a forward calculation-based optimization using a parameterized structure model (green trace). On the other hand, one can compare the obtained experimental data to a forward calculation based on the desired nanostructure or data from a golden or reference sample to probe for relevant process deviations (blue trace). In any case, the sample can be used for complementary metrology as the SF-GEXRF technique is nondestructive.

2.1. GEXRF for Nanostructure Qualification

Following the blue trace, we show that SF-GEXRF provides similar sensitivities and information about the nanostructure under investigation as compared to GIXRF by using a pre-characterized nanostructure as a golden sample and compare it to SF-GEXRF data. We use an array (1 mm × 15 mm large) of Cr nanostructures, which are nominally 300 nm × 300 nm × 20 nm (width × length × height) sized squares with a period of 1 µm in both directions. The GIXRF based characterization[30,31] of the sample allowed for a reconstruction of the dimensional properties of the Cr structure. As the identical structural model must also well-describe the GEXRF experimental data taken on the same sample, one can now directly plot the GEXRF data against a calculation using the very same parameters exchanging only the incident photon energy to the Cr-Kα fluorescence line energy. The resulting calculated curves are shown in comparison to GEXRF experimental data in Figure 2b and clearly show a good agreement considering the signal noise level (discussed in the Experimental Section) of the experimental data. In the model, a perfect box profile was assumed. However, the actual samples show rounded edges leading to minor deviations between measurement and calculation. Also the angular divergence imposed due to the size of each pixel was not considered in the calculation.

2.2. GEXRF for Full Nanostructure Reconstruction

Of course, SF-GEXRF data itself can also be used for a direct reconstruction of the nanostructures dimensional and compositional properties thus following the green trace in Figure 2a). This is demonstrated by employing a TiO_2 nanograting on silicon, which was coated with HfO_2 after etching. For this sample structure, the TiO_2 was overetched rather deep into the silicon. As a result, we obtain silicon fin-like structures with a TiO_2 tip, which is shown in **Figure 3**e, where a cross section of the grating is shown with color coded materials. The grating structure was parameterized as follows: the TiO_2-line height (h) and its width (w) and the sidewall angle (swa) describe the TiO_2, the overetch depth (o, defined from the original Si/SiO_2 surface downward) and a second sidewall angle to account for a different etch anisotropy within the Si describe the Si groove and the thicknesses of the HfO_2 and SiO_2 layer. The experimental GEXRF fluorescence maps for Ti-Kα and Hf-Lα show very distinct intensity modulations depending on the exit angles as shown in the left sides of Figure 3a,b. To speed up

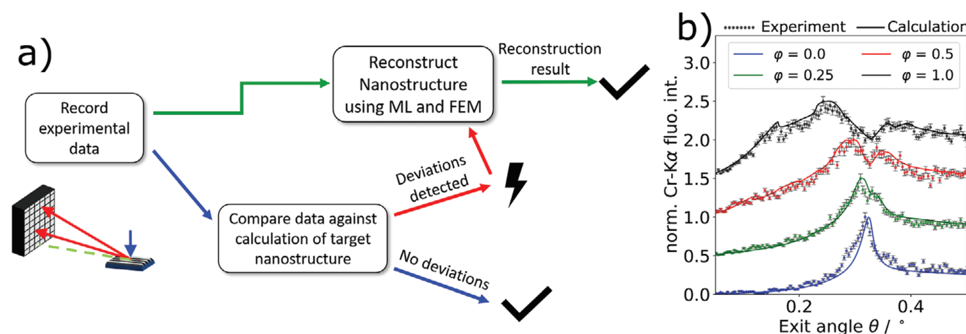

Figure 2. a) A flow chart on how SF-GEXRF data can be interpreted: One can either reconstruct the experimental datasets using machine learning (ML) and the finite element method (FEM) in order to obtain compositional and dimensional parameters or one only compares the data against a calculation for a target or reference structure to check for deviations. b) We follow the blue trace by comparing the SF-GEXRF experimental data obtained on well-characterized Cr nanostructures to a corresponding calculation. The calculation is based on a GIXRF reconstructed model (see text, vertically shifted for clarity). The error bars correspond to the counting statistics of the experimental data as well as a contribution due to the background removal.

© 2021 The Authors. Small published by Wiley-VCH GmbH

16136829, 2022, 6, Downloaded from https://onlinelibrary.wiley.com/doi/10.1002/smll.202105776 by EVIDENCE AID - BELGIUM, Wiley Online Library on [17/01/2023]. See the Terms and Conditions (https://onlinelibrary.wiley.com/terms-and-conditions) on Wiley Online Library for rules of use; OA articles are governed by the applicable Creative Commons License

16136829, 2022, 6, Downloaded from https://onlinelibrary.wiley.com/doi/10.1002/smll.202105776 by EVIDENCE AID - BELGIUM, Wiley Online Library on [17/01/2023]. See the Terms and Conditions (https://onlinelibrary.wiley.com/terms-and-conditions) on Wiley Online Library for rules of use; OA articles are governed by the applicable Creative Commons License

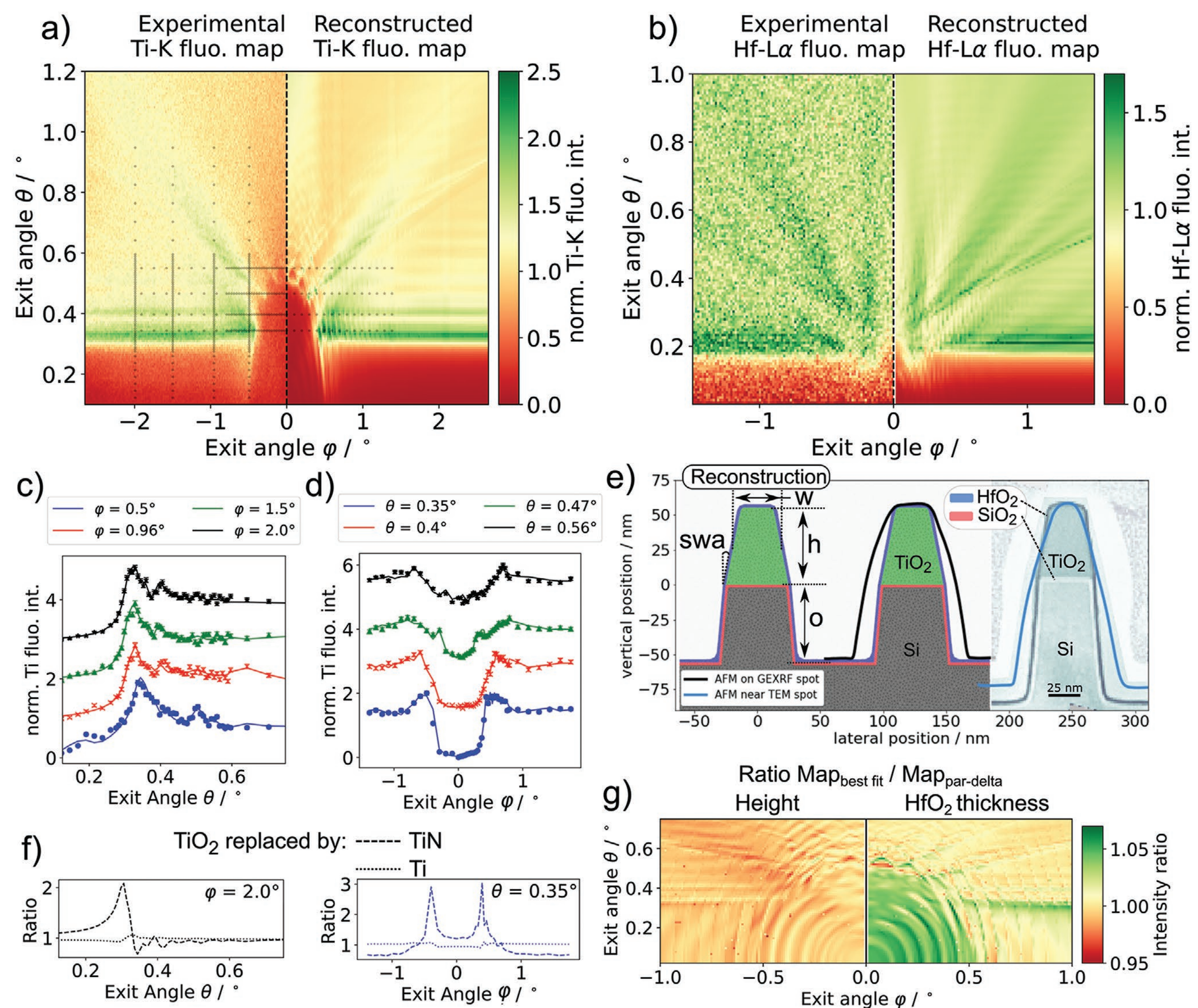

Figure 3. Comparison of the experimental GEXRF data obtained on the TiO_2-HfO_2 nanograting. a) A direct comparison of the experimental and calculated fluorescence maps for Ti-Kα fluorescence. b) A comparison of the experimental Hf-Lα fluorescence map and a calculation based on the reconstructed model of the nanostructure. c,d) The actual data points in θ and φ (from the Ti-Kα fluorescence map in (a), where the coordinates are marked with black dots) that have been used for the reconstruction and the corresponding model curves (vertically shifted for clarity). The error bars correspond to the counting statistics of the experimental data as well as a contribution due to a background removal. e) The reconstructed cross section of the nanostructure (including a sketch for definition of the model parameters and the color-coded materials), an overlay with AFM data (black solid line), as well as a comparison to a TEM cross section and corresponding AFM data (blue solid line) of a witness sample. f) exemplary calculations for the compositional sensitivity for one curve each from (c) and (d). The ratios of the reconstructed nanostructure and a dimensionally identical structure with TiO_2 replaced with either Ti or TiN are shown. g) Ratios for calculated fluorescence maps based on the reconstructed grating model and maps for which the respective model parameter has been varied by its respective modeling error (see Table 1).

the reconstruction, only a small selection of coordinates from the Ti-Kα data (indicated with black dots in Figure 3a) was used for the χ^2 minimizing reconstruction (as described in the Experimental Section). During the reconstruction procedure, the various parameters are optimized to best match the selected experimental data points in order to determine an optimal set of parameters for the nanostructure.

In Figure 3a, the calculated fluorescence map based on this final reconstruction result is shown on the right side. Although statistical noise and the angular divergence due to the finite pixel size are omitted in the calculation, the maps agree very well with respect to features present and the relative signal intensities. Four line cuts in φ and θ directions are used in the reconstruction algorithm as shown in Figure 3c,d in comparison to the final reconstruction model calculations (solid lines). Only the Ti fluorescence data was used in the reconstruction as the experimental Hf data is too noisy. Still, there is a pronounced discrimination capability for the HfO_2 layer thickness and density. This was already observed for GIXRF[31] and is due to the very short decay length of the X-ray standing wave

 © 2021 The Authors. Small published by Wiley-VCH GmbH

Table 1. Overview of the reconstructed parameters of the grating model including their respective calculated 1σ modeling parameter confidence intervals according to ref. [37]. For clarity, some of the parameters are also depicted in Figure 3e.

Model parameter	Reconstr. value	Confid. int.	Unit
Lineheight (h)	55.3	0.5	nm
Linewidth (w)	37.7	0.3	nm
HfO_2 thickn.	2.3	0.08	nm
Sidewall angle (swa)	12.4	0.3	degree
Sidewall angle Si	5.6	0.3	degree
Overetch depth (o)	−55.7	1.4	nm

field at shallow exit angles. Thus, a comparison of experimental and calculated fluorescence maps for Hf (based on the reconstructed model) shows nicely agreeing angular features (see Figure 3b).

From the employed machine learning optimization algorithm based on BO, one can calculate the confidence intervals (CI) for each parameter as demonstrated in ref. [37]. Assuming Gaussian distributed model parameters, the CI can be computed by inverting the hessian matrix filled with all second derivatives at the determined global optimum. The CI allow to assess the discrimination capability of the methodology for the respective parameter and this nanostructure. For the shown reconstruction, both the reconstructed parameters as well as their CI are listed in **Table 1**. They indicate a sub-nm discrimination capability for typical parameters of interest, for example, line heights, line width, and the HfO_2 layer thickness. For the large overetching depth, also a decent sensitivity is found even though no direct relation of the modeled Ti fluorescence is available. Thus, this methodological sensitivity is only a result of the etch depths influence on the X-ray standing wave distribution and is expected to drastically increase if, for example, also the hafnium or oxygen fluorescence from the native SiO_2 layer were used in the reconstruction. For a verification, that the calculated model parameter CI are in a reasonable order of magnitude, two ratios of calculated Ti fluorescence maps are shown in Figure 3g. Here, the calculated 2D map for the optimal reconstruction is divided by a 2D map for which only the corresponding model parameter was changed by its derived CI. These parameter variations result in local relative changes of several percent and of the general $\theta-\varphi$ dependencies. Thus, discrimination capabilities to such changes between samples are provided if the noise level of the experimental data can be reduced (to be discussed in Conclusion and Experimental Section).

As already stated, the methodology also provides elemental sensitivity with respect to the composition of the materials employed. For the presented example, this refers mainly to the stoichiometry of the oxide materials involved. It is provided through a change in the composition dependent optical constants of each material and the fluorescence maps for all elements in the nanostructure, which will differ if their spatial distribution is not equal.[30] As we are limited to only the Ti fluorescence signal here for technical reasons, we assumed stoichiometric oxides[38,39] and thus fixed the compositions. For demonstration purposes we also performed the calculations for the final reconstruction result after replacing the TiO_2 with metallic Ti or TiN and plot the ratio of the TiO_2 calculation and the replacement one in Figure 3f for two exemplary cuts. As can be seen, there are minor changes to the calculation result for the metallic Ti but rather large changes if TiN is considered. This compositional sensitivity can be even enhanced if the fluorescence radiation of all elements in the compound is detected or measured in an absolute manner. This requires the use of soft X-ray capable detectors or calibrated detectors but would enable a reconstruction of the stoichiometry.

Finally, one can compare the reconstructed cross section of the grating to other metrology techniques, for example, AFM or TEM for validation purposes. In Figure 3e, a comparison to an AFM profile obtained in the vicinity of the GEXRF experimental location is shown in the center part of the figure as a black solid line. Due to the interplay of the tip shape with the nanostructure, the AFM line profiles seem wider. But the absolute height (112 nm, difference of groove between grating lines and top) matches the GEXRF result very well. Also, a comparison to a TEM cross section, which was prepared far away (about 7 mm) from the GEXRF measurement location to not contaminate the sample is shown on the right side. Here it should be noted that the homogeneity of the pattern transfer etch was less perfect toward the edges of the structured area (1 mm by 15 mm large stripe) and thus the TEM preparation spot is to be considered as a witness sample. Consequently, the TEM reveals much deeper overetch and a thinner grating line which is also found by performing AFM in this region of the sample (blue solid line). Nevertheless, the TEM also allows to identify the different materials in the nanostructure showing a very good agreement to our reconstruction result. Also the TEM derived height of the TiO_2 (56 nm) and thickness of the HfO_2 (2.5 nm) agree very well.

2.3. Compatibility to Realistic Test Field Sizes

The biggest benefit of the GEXRF geometry is the straightforward reduction in excitation footprint size on the sample. Thus, the much smaller test fields on dies from, for example typical semiconductor processing studies become directly accessible and no dedicated mm^2 sized large area fields are required as for grazing-incident techniques. And even for nanostructures where large areas can be coated, the superior lateral resolution of GEXRF enables position dependent studies, for example, to probe homogeneity. As a showcase, we are using state of the art vertical gate-all-around nanowire (NW) field effect transistor structures as shown in **Figure 4**d,e. Here, the NWs of interest are fabricated on a 500 µm × 500 µm large area, which is surrounded by NWs with different diameter and pitch and other nanostructures. Thus, any kind of grazing incidence experiment cannot be performed as they would suffer from overlapping signals from adjacent structures due to the large footprint. By employing the SF-GEXRF approach, we can easily reduce the effective size of the exciting X-ray beam on the sample from several mm^2 to 400 µm × 400 µm in this case and position it to only irradiate the area of interest. For the present example, we do not need to use any focusing optic as the test field is large enough in size to shape the beam with the exit slits in the

 © 2021 The Authors. Small published by Wiley-VCH GmbH

16136829, 2022, 6, Downloaded from https://onlinelibrary.wiley.com/doi/10.1002/smll.202105776 by EVIDENCE AID - BELGIUM, Wiley Online Library on [17/01/2023]. See the Terms and Conditions (https://onlinelibrary.wiley.com/terms-and-conditions) on Wiley Online Library for rules of use; OA articles are governed by the applicable Creative Commons License

16136829, 2022, 6, Downloaded from https://onlinelibrary.wiley.com/doi/10.1002/smll.202105776 by EVIDENCE AID - BELGIUM, Wiley Online Library on [17/01/2023]. See the Terms and Conditions (https://onlinelibrary.wiley.com/terms-and-conditions) on Wiley Online Library for rules of use; OA articles are governed by the applicable Creative Commons License

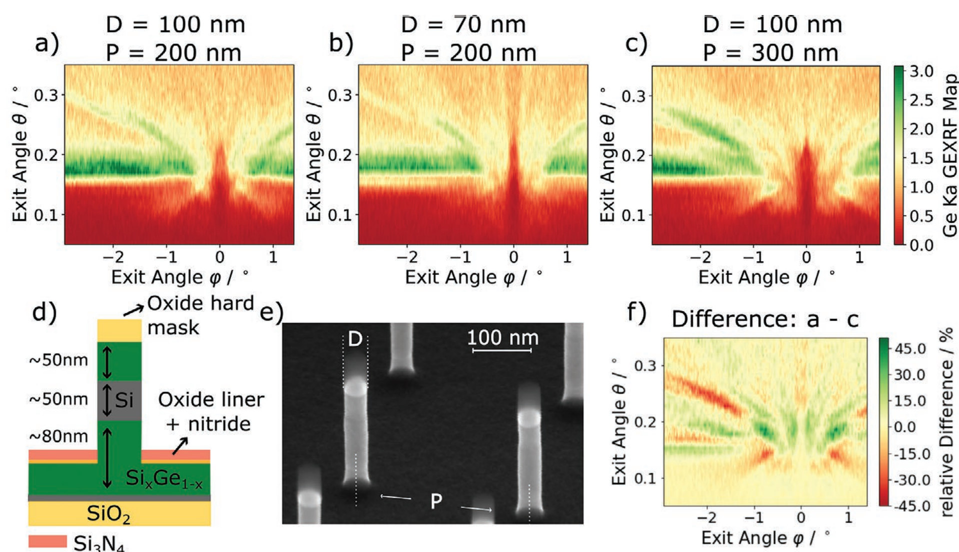

Figure 4. Comparison of three experimental GEXRF datasets for Ge-Kα fluorescence radiation from different SiGe nanowire structures with a,b) varying diameter and a,c) varying pitch fabricated on small (500 µm × 500 µm) test fields surrounded by other structures. d) The nominal cross section as well as e) an SEM image are also shown. For demonstration purposes, also f) the difference map for the varying pitch datasets is shown.

beamline. But also, smaller test field sizes would be feasible for such GEXRF characterization as the exciting X-ray beam can be easily focused to below 50 µm using, for example, poly capillary lenses or single-bounce optics.

Experimental fluorescence maps of the Ge-Kα fluorescence line from three different NW structures with varying diameter (100 and 70 nm, Figure 4a,b) and varying pitch (200 and 300 nm, Figure 4a,c) are shown in comparison. As shown, the general θ and φ dependence of the fluorescence maps does substantially change and distinct differences are observable for the different structure parameters. For additional demonstration that the SF-GEXRF technique provides high discrimination capability to these structural parameters, a difference map between the pitch 200 nm and the pitch 300 nm NWs is shown in Figure 4f. The example shows that the SF-GEXRF technique can be applied to industrial 3D nanostructures on typical metrology pads on the die. Due to relatively low amount of Ge present in the nanostructure as well as a nonoptimized excitation (see Experimental Section), the noise level of the obtained data is not sufficient for a reliable reconstruction. However, as discussed later (see Conclusion), this is not a general limitation of the technique and could be well improved if a dedicated experimental setup is used.

2.4. Compatibility with Laboratory X-Ray Sources

Finally, a potential 3D nanometrology technique will be most beneficial for application if it can be performed directly at the respective laboratory and no access limited large-scale research facilities are required. Even though the presented main developments of the SF-GEXRF technique have been performed using synchrotron beamlines as excitation sources, the technique is suitable for laboratory-based application. Laboratory based application examples of GEXRF already exist[40] and naturally also the SF-GEXRF based nanostructure characterization can be performed employing such setups. For a demonstration, we used a low power microfocus X-ray tube as well as a pnCCD (p-n junction charge coupled device)[41] as the area selective fluorescence detector to perform GEXRF on the Cr nanostructures shown earlier. The thereby obtained data for Cr-Kα fluorescence is shown in **Figure 5** in comparison to the already shown calculated data as well as a corresponding synchrotron based experimental dataset.

Even though, the laboratory-based experimental data is somewhat noisy due to limited integration time and inefficient excitation of the Cr structures (only bremsstrahlung from a Rh tube was available, see Experimental Section for further details), the expected intensity behavior is clearly visible when comparing the calculated and experimental $\theta-$φ maps. Considering the fact, that several optimizations to speed-up the experiment could easily be employed in a dedicated experimental setup, such experiments are clearly feasible also on easy-to-access laboratory instruments.

3. Conclusion

In the present work, we introduce and apply the SF-GEXRF technique for a reliable quantitative dimensional and analytical or compositional characterization of 2D and 3D nanostructures. By changing the geometry from grazing incidence to grazing exit, we successfully achieved similar discrimination capabilities as compared to GIXRF. However, in grazing exit geometry the incident beam footprint is much smaller and thus small sized nanostructured areas are accessible. This enables applications, for example, for semiconductor related topics, where test fields are sized in the order of 500 µm × 500 µm or smaller. It also allows for a reasonably high spatial resolution, for example, to probe homogeneity for large area nanostructure arrays. Furthermore, we have proven that the SF-GEXRF technique is also feasible using laboratory-based instruments to which access is much easier as compared to large scale research facilities.

© 2021 The Authors. Small published by Wiley-VCH GmbH

16136829, 2022, 6, Downloaded from https://onlinelibrary.wiley.com/doi/10.1002/smll.202105776 by EVIDENCE AID - BELGIUM, Wiley Online Library on [17/01/2023]. See the Terms and Conditions (https://onlinelibrary.wiley.com/terms-and-conditions) on Wiley Online Library for rules of use; OA articles are governed by the applicable Creative Commons License

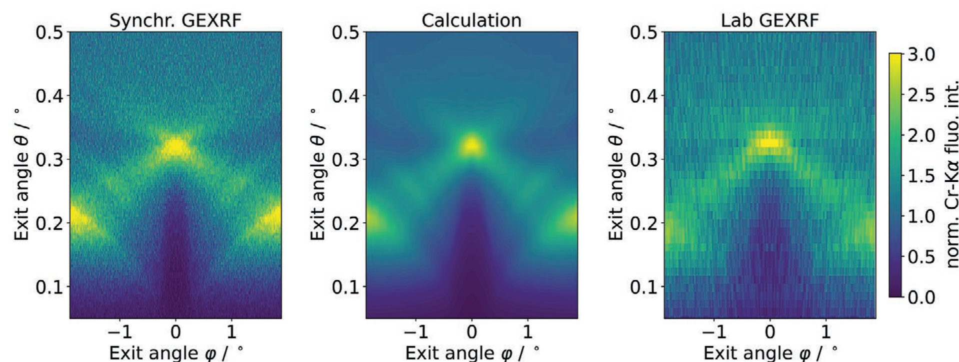

Figure 5. Comparison of the synchrotron-based dataset (left) and the calculation (center) to the experimental GEXRF data (right) taken using a non-synchrotron-based laboratory setup employing a low power microfocus X-ray tube and a pnCCD detector for the 3D Cr nanostructure. Even though, the experimental setup employed was not at all optimized for this application, the obtained data is clearly showing feasibility.

As we have shown, a full reconstruction of relevant dimensional and compositional parameters of the nanostructure can be performed providing statistically relevant results from many nanoobjects at once in a nondestructive manner. Here, the nanostructures are probed without the need for cross-sectioning, lamella preparation or other preparative work. In contrast to, for example, SEM, also buried parts of the nanostructure are accessible if overlayers are not thicker than the penetration dynamic range of the X-ray standing wave (in the order of 10–50 nm). In addition, also the characterization of inhomogeneities or in-depth gradients within the nanostructure, for example for doping profiles, can be characterized if a reasonably high fluorescence emission from the respective marker element and thus a reasonably high concentration of this element is present in the nanostructure. The information retrieved from GEXRF reconstruction shows good agreement to AFM and TEM data, which could be performed on the same spot due to the nondestructive nature of GEXRF. It should also be noted, that one can of course also apply the scanning-free GEXRF technique to randomly ordered nanostructures. As shown for GIXRF,[42] this simplifies the required reconstruction but it is expected to provide less dimensional discrimination capability as there is no azimuthal angle dependence of the fluorescence signals for disordered structures.

Considering these initial "proof-of-principle" experiments, the technique is rather slow as both the data acquisition and the parameter reconstruction as performed here require several hours. But, especially on the experimental side, the employed setups offer a large optimization potential for the SF-GEXRF applications. Employing a dedicated experimental setup, there is room for drastic decreases in time-to-data by, for example, a more efficient fluorescence excitation (monochromatic instead of white-light) and less overhead during detection (faster readout CMOS or pnCCD detectors instead of CCDs). A conservative estimate for the case of the SiGe-NWs and a monochromatic excitation[43] instead of the one used here provides a reduction of required integration time by a factor of about 40. Additionally, CMOS or pnCCD detectors would also allow to detect soft-X-ray radiation from, for example, oxygen to be more sensitive for elemental compositions in the nanostructure. A combined reconstruction of different elements fluorescence data will further increase the achievable parameter sensitivites.[37] The reconstruction related computational load can be handled by employing more powerful computers. If only the evolution of critical parameters across different samples are to be monitored, one could also employ much faster mathematical approaches to speed up the reconstruction, for example, polynomial chaos expansion.[44] But even without these future developments, the presented technique can substantially contribute to the metrology needs in nanotechnology where 2D and 3D structures must be well-controlled with respect to their dimensions and composition.[21,23]

4. Experimental Section

Fabrication of Chromium Nanostructures: As a simple example for 3D nanostructures, an array of chromium cuboids with a nominal dimension of 300 nm × 300 nm × 20 nm (width × length × height) was used on a 300 nm SiO_2 layer on Si substrate. They were prepared on an area of 1 × 15 mm^2 using the electron beam lithography (EBL) technique. Each nanostructure had thus a reasonable identical nominal square shape and dimension. Further details about the fabrication procedure can be found in ref. [42]. As these nanostructures are provided on a reasonably large area, they were also characterized using the reference-free GIXRF technique (further details and results of these experiments can be found in ref. [31]). From a reconstruction of the GIXRF data, the dimensional and compositional parameters were retrieved, and the very same parameters must also describe the GEXRF data. Thus, their expected response for the employed SF-GEXRF based experiment detecting the Cr-Kα fluorescence can readily be calculated using the same parameter set employing the MB-DDT[30] calculation approach.

Fabrication of Titanium Oxide Nanograting: For the experiments, TiO_2 gratings with a period of 123 nm were fabricated on a polished and cleaned silicon wafer. They were prepared on an area of 1 × 15 mm^2 using the character projection EBL technique. The native oxide was removed by ion beam etching (Oxford Ionfab 300+LC) and subsequently 50 nm TiO_2 was deposited by means of ion beam sputtering from a titanium target with ambient oxygen and finally 15 nm of chromium was deposited as material for the later hard mask. Then, the pattern was generated by character projection EBL (Vistec SB350 OS) in a negative tone resist (TOK OEBR-CAN038). This structure was then transferred into the chromium layer by means of reactive ion etching (RIE, Sentech Si-591) utilizing a 5:1 mixture of chlorine and oxygen. After oxygen plasma striping of the resist mask, an inductive coupled plasma etching procedure (Sentech Si-500-C) was used to transfer the pattern into the titanium dioxide layer utilizing tetrafluoromethane as process gas at a substrate temperature of −50° C. Afterward, the chromium hard mask was wet chemically removed. In the next step 18 cycles of

 © 2021 The Authors. Small published by Wiley-VCH GmbH

HfO_2 were conformably coated onto the structure by means of atomic layer deposition (SENTECH SILAYO PEALD System) using TDMAH (Tetrakis(di-methylamino)hafnium) and O_2-plasma as precursors.[45]

Due to the large area surrounding the actual nanostructure, RIE lag occured due to a local depletion of the etch species. In conjunction with the significantly higher etch rate of Si as compared to the titanium oxide, which causes the high overetch into the Si, the resulting etch rate gradient explained the different overetch depths between the position of the TEM image and the GEXRF measurement.

Fabrication of SiGe-Nanowire Structures: As a technologically more relevant nanostructure, a test die was used for vertical GAA NW field-effect transistors from imec.[26] Among other types of structures, this test die contained several 500 µm × 500 µm large fields with dimensionally different nanowire structures. The main differences between NWs was a changing diameter or pitch. Here, three stacked layers (SiGe, Si, SiGe) were grown epitaxially and subsequently patterned into pillars, such that a vertical Si channel region (grey in of Figure 4d) was sandwiched by the highly boron doped SiGe source and drain (dark green in Figure 4d).

Synchrotron Based Scanning-Free GEXRF: The SF-GEXRF experiments on the Cr nanostructures (Figure 2), the TiO_2 nanostructures (Figure 3) and the SiGe/Si/SiGe Nanowires (Figure 4) were performed using a CCD as position sensitive detector and an existing experimental chamber optimized for GIXRF experiments.[46] The setup was mounted at PTB's white light dipole beamline,[47] which provided undispersed dipole radiation. For a rough optimization of the excitation conditions for Cr, Hf, and Ge, different filters can be placed in the beam to block the low photon energy part of the spectrum. The beam size as well as the incident photon flux can be controlled using slits. The sample to be investigated was aligned with respect to the incident beam and the CCD detector to ensure a 90° incident angle as well as to have the 0° exit angle position in both θ and φ direction optimally positioned on the CCD. In addition to the position sensitivity, one can also take advantage of the reasonably high photon energy resolution of CCD detectors.[48] Even though this limited the number of total events that can be detected in one CCD frame, it allowed to measure the GEXRF fluorescence maps of several different chemical elements present in the sample at the same time. For reasonable counting statistics in the overall fluorescence map, many images must be taken and evaluated by isolating events within the respective region of interest in the histogram (see ref. [48]). Here, overall integration times were in the order of about 40 h, due to several limitations imposed by the available instrumentation. On the excitation side, the employed beamline was relatively inefficient as the main part of the incident photon energy spectrum did not contribute to fluorescence production or only with very low cross sections for the targeted elements. Here, monochromatic excitation would reduce the integration time by a factor between 20 and 40 depending on the beamline to be used and the element of interest. In addition, the distance between the CCD detector and the sample was fixed at a relatively large distance of ≈350 mm resulting also in much lower than necessary solid angles of detection for each pixel.

The pixel coordinates of the CCD can be transferred to mean angular positions for θ and φ using the overall distance between CCD and the irradiation spot on the sample and the pixel size. This was supported by measuring both known nonstructured layer samples and the reflected incident beam at smaller incident angles. The detected number of events in each pixel where also corrected for each pixel's solid angle of detection, which slightly changed across the CCD. The relative detection efficiencies of the pixels were cross checked by performing flat field measurements at large θ exit angles and found to be negligible.

Laboratory Based Scanning-Free GEXRF: The employed laboratory setup was consisting of a low power X-ray tube (XOS flex beam 50 W microfocus Xray tube with a Rh target), a sample holder and an pnCCD (p-njunction charge coupled device)[41] as the detector. Here, the pnCCD provided simultaneous position- and energy-dispersive detection of X-rays at much higher read-out rates as compared to conventional CCD detectors, but the experiment would also be possible employing CCD or even CMOS based[49] 2D detectors.

The detection geometry of the setup was aligned to ensure having the 0° position in both θ and φ direction optimally positioned on the detector. The incident beam geometry was slightly different as compared to the synchrotron setup as the X-ray tube was equipped with a poly capillary lens to focus the beam onto the sample. In addition, the incident angle toward the surface of the Cr nanostructure sample was chosen to be much lower than 90° due to instrumental constraints. The distance between the irradiated spot on the sample and the pnCCD detector was about 260 mm.

The integration time was about 50 h (which was comparable to the previously shown synchrotron-based experiments), allowing for decent counting statistics in each pixel. For this very simple proof-of-principle experimental setup and limited time, the distance between the excitation spot on the sample and the pnCCD detector could not be measured at sufficient accuracy. In addition, the detector could not be positioned to be perfectly align with respect to its angles toward the plane of the sample surface as well as the plane of incidence. As a result, these necessary geometrical parameters of the setup and thereby the exit angular axes were derived by optimizing the match to the GEXRF calculation. However, the good agreement between the laboratory GEXRF data taken and the calculation clearly demonstrated this feasibility of such experiments on laboratory scale instruments. The required geometrical optimizations can easily be performed in a dedicated experimental setup.

Modeling Schemes: For a GIXRF based characterization of such nanostructures, two different modeling schemes have been applied so far. On the one hand, finite element-based solvers of the Maxwell equations[29,32] were well-suited for periodic nanostructures but they required a high computational effort. This was especially a bottleneck if 3D nanostructures were to be calculated. On the other hand, the so-called MB-DDT,[30] which allowed to derive a semi-analytical solution to the Sherman equation[50] in a linear-algebraic form. The semi-analytic solution drastically reduced the necessary computational resources as compared to the FEM approach. However, in this approach the sample was at present approximated as a stack of box-shaped structures which limited the complexity of the sample model contrary to the FEM-based scheme.

For both the FEM- and the MB-DDT based reconstruction, the nanostructure was first parameterized to allow for automatic optimization. Using the TiO_2-HfO_2 nanograting example, this resulted for instance in a 2D cross-section of the grating line, where parameters as the line width and height, the native SiO_2 and ALD-coated HfO_2 layer thicknesses, the overetch depth, as well as the sidewall angles of the grating line and the etched silicon served as optimization parameters. The corresponding calculation domain for the FEM is shown in Figure 3e. For the MB-DDT based modeling of the GIXRF data of the 3D Cr nanostructures the dimensions of the Cr boxes (height and width) and the thickness of a surface oxide layer was used. Further details can be found in ref. [31]. By using a machine learning algorithm such as BO[51] or others, an optimal set of the model parameters can then be reconstructed. On a 40-core Intel Xeon rack, the shown reconstruction of the TiO_2-HfO_2 nanograting took about 100 h to converge.

Microscopy Experiments: For a validation of the GEXRF reconstruction of TiO_2-HfO_2 nanograting, additional AFM measurements were performed with an Nanosurf Nanite 25×25. The sample was measured under tapping mode condition and a standard pyramidal shaped silicon probe with a tip radius <10 nm was used.[52] The AFM-probe was characterized by a resonance frequency of 190 Hz and force constant of 48 N m^{-1}. Several line scans across the nanostructured area were performed to investigate the homogeneity of key grating parameters. The superposed AFM line profiles in Figure 3e are from the center of the nanostructured area (black line), where also the GEXRF measurements were performed and from the edge of the structured area (blue line), where the TEM lamella was taken from. The increased overetch depth as well as the narrower line shape from the TEM versus GEXRF comparison can also be found comparing the two AFM line scans and were thus due to the sample inhomogeneity.

Furthermore, high-resolution TEM and scanning TEM were carried out using a JEOL NEOARM 200F operating at 200 kV. The device was equipped with a cold field emission gun, 4k × 4k CCD-camera (Gatan

© 2021 The Authors. Small published by Wiley-VCH GmbH

16136829, 2022, 6, Downloaded from https://onlinelibrary.wiley.com/doi/10.1002/smll.202105776 by EVIDENCE AID - BELGIUM, Wiley Online Library on [17/01/2023]. See the Terms and Conditions (https://onlinelibrary.wiley.com/terms-and-conditions) on Wiley Online Library for rules of use; OA articles are governed by the applicable Creative Commons License

OneView) and a windowless double SDD with a total detector area of 200 mm^2 (JEOL centurio) for energy dispersive X-ray analysis. The TEM lamella preparation was performed at an FEI Helios NanoLab G3 UC. At first the surface was protected by a layer stack locally applied with beam induced chemical vapor deposition. The stack was formed by e-beam induced carbon deposition followed by e-beam induced platinum deposition followed by Ga-beam induced carbon deposition. Subsequently a lamella with a thickness of 1.5 µm was cut out using 30 keV Ga ion beam and welded on both ends to a copper TEM lift-out grid using sputter deposition. The final thinning was performed using 30 keV Ga ions with a current of 80 pA down to a thickness of less than 100 nm. Afterward low energy polishing with 5 keV and finally 2 keV Ga ions was used to reduce ion beam induced damage.

Acknowledgements

The authors would like to thank Vivek Rameshbhai Beladiya and Adriana Szeghalmi for depositing the HfO_2-ALD deposition. Parts of this research was performed within the EMPIR projects Aeromet II and Adlab-XMet. The financial support of the EMPIR program is gratefully acknowledged. It is jointly funded by the European Metrology Programme for Innovation and Research (EMPIR) and participating countries within the European Association of National Metrology Institutes (EURAMET) and the European Union. In addition, this project has received funding from the Electronic Component Systems for European Leadership Joint Undertaking under grant agreement No 826589–MADEin4. This joint undertaking receives support from the European Union's Horizon 2020 research and innovation programme and Netherlands, France, Belgium, Germany, Czech Republic, Austria, Hungary, Israel. K.N. acknowledges the funding by the RFBR, project number 19-29-12038. A.U. and M.R. also gratefully acknowledge financial support by DFG (Inst 275/391-1). imec gratefully acknowledges the financial support by FWO-Hercules through project AKUL/15/22.

Open access funding enabled and organized by Projekt DEAL.

Conflict of Interest

The authors declare no conflict of interest.

Data Availability Statement

Research data are not shared but can be made available from the corresponding author upon reasonable request.

Keywords

dimensional and compositional analysis, grazing exit X-ray fluorescence, machine learning, nanostructure characterization

Received: September 21, 2021
Revised: October 20, 2021
Published online: November 25, 2021

[1] M. Akbari-Saatlu, M. Procek, C. Mattsson, G. Thungström, H.-E. Nilsson, W. Xiong, B. Xu, Y. Li, H. H. Radamson, *Nanomaterials* **2020**, *10*, 2215.
[2] S. Kasani, K. Curtin, N. Wu, *Nanophotonics* **2019**, *8*, 2065.
[3] J. S. T. Smalley, F. Vallini, S. A. Montoya, L. Ferrari, S. Shahin, C. T. Riley, B. Kanté, E. E. Fullerton, Z. Liu, Y. Fainman, *Nat. Commun.* **2017**, *8*, 13793.
[4] W. Wang, L. Qi, *Adv. Funct. Mater.* **2019**, *29*, 1807275.
[5] R. Pala, J. Liu, E. Barnard, D. Askarov, E. Garnett, S. Fan, M. Brongersma, *Nat. Commun.* **2013**, *4*, 2095.
[6] M. Khraiche, R. E. Hassan, *J. Sci.: Adv. Mater. Devices* **2020**, *5*, 279.
[7] Y.-S. Duh, Y. Nagasaki, Y.-L. Tang, P.-H. Wu, H.-Y. Cheng, T.-H. Yen, H.-X. Ding, K. Nishida, I. Hotta, J.-H. Yang, Y.-P. Lo, K.-P. Chen, K. Fujita, C.-W. Chang, K.-H. Lin, J. Takahara, S.-W. Chu, *Nat. Commun.* **2020**, *11*, 4101.
[8] L. Romano, M. Kagias, J. Vila-Comamala, K. Jefimovs, L.-T. Tseng, V. Guzenko, M. Stampanoni, *Nanoscale Horiz.* **2020**, *5*, 869.
[9] L. Peixoto, R. Magalhães, D. Navas, S. Moraes, C. Redondo, R. Morales, J. P. Araújo, C. T. Sousa, *Appl. Phys. Rev.* **2020**, *7*, 011310.
[10] S. Han, H. Kim, Y. Kim, Y.-J. Kim, S. Kim, I.-Y. Park, S.-W. Kim, *Nat. Commun.* **2016**, *7*, 13105.
[11] G. Moore, *Electronics* **1965**, *38*, 114.
[12] R. Clark, *Materials* **2014**, *7*, 2913.
[13] S. King, H. Simka, D. Herr, H. Akinaga, M. Garner, *APL Mater.* **2013**, *1*, 040701.
[14] S. Natarajan, M. Agostinelli, S. Akbar, M. Bost, A. Bowonder, V. Chikarmane, S. Chouksey, A. Dasgupta, K. Fischer, Q. Fu, T. Ghani, M. Giles, R. G. S. Govindaraju, W. Han, D. Hanken, E. Haralson, M. Haran, M. Heckscher, R. Heussner, P. Jain, R. James, R. Jhaveri, I. Jin, H. Kam, E. Karl, C. Kenyon, M. Liu, Y. Luo, R. Mehandru, S. Morarka, et al., in *2014 IEEE International Electron Devices Meeting (IEDM)*, IEEE, Piscataway, NJ **2014** pp. 3.7.1–3.7.3.
[15] R. R.-H. Kim, S. Sherazi, P. Debacker, P. Raghavan, J. Ryckaert, A. Malik, D. Verkest, J. Lee, W. Gillijns, L. Tan, V. Blanco, K. Ronse, G. McIntyre, In *Design-Process-Technology Co-Optimization for Manufacturability XII*, (Eds: J. P. Cain, C.-M. Yuan), SPIE, Bellingham, WA **2018**.
[16] A. Vandooren, J. Franco, Z. Wu, B. Parvais, W. Li, L. Witters, A. Walke, L. Peng, V. Deshpande, N. Rassoul, G. Hellings, G. Jamieson, F. Inoue, K. Devriendt, L. Teugels, N. Heylen, E. Vecchio, T. Zheng, E. Rosseel, W. Vanherle, A. Hikavyy, G. Mannaert, B. T. Chan, R. Ritzenthaler, J. Mitard, L. Ragnarsson, N. Waldron, V. D. Heyn, S. Demuynck, J. Boemmels, D. Mocuta, J. Ryckaert, N. Collaert, in *2018 IEEE International Electron Devices Meeting (IEDM)*, IEEE, Piscataway, NJ **2018**, pp. 7.1.1–7.1.4.
[17] J. Ryckaert, P. Schuddinck, P. Weckx, G. Bouche, B. Vincent, J. Smith, Y. Sherazi, A. Mallik, H. Mertens, S. Demuynck, T. H. Bao, A. Veloso, N. Horiguchi, A. Mocuta, D. Mocuta, J. Boemmels, in *2018 IEEE Symposium on VLSI Technology*, IEEE, Piscataway, NJ **2018**, pp. 141–142.
[18] S. Dey, J. Jena, E. Mohapatra, T. Dash, S. Das, C. Maiti, *Phys. Scr.* **2019**, *95*, 014001.
[19] B. Bunday, in *Metrology, Inspection, and Process Control for Microlithography XXX*, (Eds: M. I. Sanchez, V. A. Ukraintsev), vol. *9778*, SPIE, Bellingham, WA **2016**, p . 97780E.
[20] B. Bunday, E. Solecky, A. Vaid, A. Bello, X. Dai, in *Metrology, Inspection, and Process Control for Microlithography XXXI*, (Eds: M. I. Sanchez, V. A. Ukraintsev), SPIE, Bellingham, WA **2017**, p. 101450G.
[21] N. G. Orji, M. Badaroglu, B. M. Barnes, C. Beitia, B. D. Bunday, U. Celano, R. J. Kline, M. Neisser, Y. Obeng, A. E. Vladar, *Nat. Electron.* **2018**, *1*, 532.
[22] C. Jun, in *Metrology, Inspection, and Process Control for Semiconductor Manufacturing XXXV* (Eds: O. Adan, J. C. Robinson), SPIE, Bellingham, WA **2021**, p. 161106.
[23] International Roadmap for Devices and Systems, Metrology, Technical Report, IEEE, Piscataway, NJ **2020**.
[24] B. Bunday, A. Bello, E. Solecky, A. Vaid, in *Metrology, Inspection, and Process Control for Microlithography XXXII* (Eds: O. Adan, V. A. Ukraintsev), SPIE, Bellingham, WA **2018**, p. 105850I.
[25] W. Vandervorst, C. Fleischmann, J. Bogdanowicz, A. Franquet, U. Celano, K. Paredis, A. Budrevich, *Mater. Sci. Semicond. Process.* **2016**.

© 2021 The Authors. Small published by Wiley-VCH GmbH

16136829, 2022, 6, Downloaded from https://onlinelibrary.wiley.com/doi/10.1002/smll.202105776 by EVIDENCE AID - BELGIUM, Wiley Online Library on [17/01/2023]. See the Terms and Conditions (https://onlinelibrary.wiley.com/terms-and-conditions) on Wiley Online Library for rules of use; OA articles are governed by the applicable Creative Commons License

[26] A. Veloso, A. Hikavyy, R. Loo, V. Paraschiv, B. T. Chan, D. Radisic, W. Li, J. J. Versluijs, L. Teugels, F. Sebaai, P. Favia, G. Eneman, H. Bender, E. Vancoille, J. E. Scheerder, C. Fleischmann, N. Horiguchi, P. Matagne, T. Huynh-Bao, A. Chasin, E. Simoen, E. Vecchio, K. Devriendt, S. Brus, E. Rosseel, in *2019 IEEE Int. Electron Devices Meeting (IEDM)*, IEEE, Piscataway, NJ **2019**, pp. 11.1.1–11.1.4.
[27] D. Melkonyan, C. Fleischmann, A. Veloso, A. Franquet, J. Bogdanowicz, R. Morris, W. Vandervorst, *Ultramicroscopy* **2018**, *186*, 1.
[28] Y. Kayser, J. Szlachetko, J. Sá, *Rev. Sci. Instrum.* **2013**, *84*, 123102.
[29] V. Soltwisch, P. Hönicke, Y. Kayser, J. Eilbracht, J. Probst, F. Scholze, B. Beckhoff, *Nanoscale* **2018**, *10*, 6177.
[30] K. V. Nikolaev, V. Soltwisch, P. Hönicke, F. Scholze, J. de la Rie, S. N. Yakunin, I. A. Makhotkin, R. W. E. van de Kruijs, F. Bijkerk, *J. Synchrotron Radiat.* **2020**, *27*, 2.
[31] P. Hönicke, A. Andrle, Y. Kayser, K. Nikolaev, J. Probst, F. Scholze, V. Soltwisch, T. Weimann, B. Beckhoff, *Nanotechnology* **2020**, *31*, 505709.
[32] S. Burger, L. Zschiedrich, J. Pomplun, S. Herrmann, F. Schmidt, in *Metrology, Inspection, and Process Control for Microlithography XXIX* (Eds: J. P. Cain, M. I. Sanchez), vol. *9424*, SPIE, Bellingham, WA **2015**, pp. 329–336.
[33] P.-I. Schneider, M. Plock, S. Burger, in *Modeling Aspects in Optical Metrology VIII* (Eds: B. M. Barnes, B. Bodermann, K. Frenner), SPIE, Bellingham, WA **2021** p. 117830J.
[34] F. Pfeiffer, *Nat. Photonics* **2017**, *12*, 9.
[35] M. Holler, M. Guizar-Sicairos, E. Tsai, R. Dinapoli, E. Müller, O. Bunk, J. Raabe, G. Aeppli, *Nature* **2017**, *543*, 402.
[36] H. Trombini, G. G. Marmitt, I. Alencar, D. L. Baptista, S. Reboh, F. Mazen, R. B. Pinheiro, D. F. Sanchez, C. Senna, B. S. Archanjo, C. A. Achete, P. Grande, *Sci. Rep.* **2019**, *9*, 11629.
[37] A. Andrle, P. Hönicke, G. Gwalt, P.-I. Schneider, Y. Kayser, F. Siewert, V. Soltwisch, *Nanomaterials* **2021**, *11*, 1647.
[38] C. Bundesmann, T. Lautenschläger, E. Thelander, D. Spemann, *Nucl. Instrum. Methods Phys. Res., Sect. B* **2017**, *395*, 17.
[39] D. Blaschke, F. Munnik, J. Grenzer, L. Rebohle, H. Schmidt, P. Zahn, S. Gemming, *Appl. Surf. Sci.* **2020**, *506*, 144188.
[40] J. Baumann, Y. Kayser, B. Kanngießer, *Phys. Status Solidi B* **2020**, 2000471.
[41] S. Send, A. Abboud, R. Hartmann, M. Huth, W. Leitenberger, N. Pashniak, J. Schmidt, L. Strüder, U. Pietsch, *Nucl. Instrum. Methods Phys. Res., Sect. A* **2013**, *711*, 132.
[42] M. Dialameh, F. F. Lupi, P. Hönicke, Y. Kayser, B. Beckhoff, T. Weimann, C. Fleischmann, W. Vandervorst, P. Dubcek, B. Pivac, M. Perego, G. Seguini, N. D. Leo, L. Boarino, *Phys. Status Solidi A* **2017**, *215*, 1700866.
[43] W. Görner, M. Hentschel, B. Müller, H. Riesemeier, M. Krumrey, G. Ulm, W. Diete, U. Klein, R. Frahm, *Nucl. Instrum. Methods Phys. Res., Sect. A* **2001**, *467–468*, 703.
[44] N. Farchmin, M. Hammerschmidt, P.-I. Schneider, M. Wurm, B. Bodermann, M. Bär, S. Heidenreich, *J. Micro/Nanolithogr., MEMS, and MOEMS* **2020**, *19*, 024001.
[45] M. Lapteva, V. Beladiya, S. Riese, P. Hanke, F. Otto, T. Fritz, P. Schmitt, O. Stenzel, A. Tünnermann, A. Szeghalmi, *Opt. Mater. Express* **2021**, *11*, 1918.
[46] J. Lubeck, B. Beckhoff, R. Fliegauf, I. Holfelder, P. Hönicke, M. Müller, B. Pollakowski, F. Reinhardt, J. Weser, *Rev. Sci. Instrum.* **2013**, *84*, 045106.
[47] B. Beckhoff, A. Gottwald, R. Klein, M. Krumrey, R. Müller, M. Richter, F. Scholze, R. Thornagel, G. Ulm, *Phys. Status Solidi B* **2009**, *246*, 1415.
[48] J. Szlachetko, J.-C. Dousse, J. Hoszowska, M. Berset, W. Cao, M. Szlachetko, M. Kavčič, *Rev. Sci. Instrum.* **2007**, *78*, 093102.
[49] T. Harada, N. Teranishi, T. Watanabe, Q. Zhou, J. Bogaerts, X. Wang, *Appl. Phys. Express* **2019**, *13*, 016502.
[50] J. Sherman, *Spectrochim. Acta* **1955**, *7*, 283.
[51] B. Shahriari, K. Swersky, Z. Wang, R. Adams, N. D. Freitas, *Proc. IEEE* **2016**, *104*, 148.
[52] F. Siewert, B. Löchel, J. Buchheim, F. Eggenstein, A. Firsov, G. Gwalt, O. Kutz, S. Lemke, B. Nelles, I. Rudolph, F. Schäfers, T. Seliger, F. Senf, A. Sokolov, C. Waberski, J. Wolf, T. Zeschke, I. Zizak, R. Follath, T. Arnold, F. Frost, F. Pietag, A. Erko, *J. Synchrotron Radiat.* **2018**, *25*, 91.

© 2021 The Authors. Small published by Wiley-VCH GmbH

16136829, 2022, 6, Downloaded from https://onlinelibrary.wiley.com/doi/10.1002/smll.202105776 by EVIDENCE AID - BELGIUM, Wiley Online Library on [17/01/2023]. See the Terms and Conditions (https://onlinelibrary.wiley.com/terms-and-conditions) on Wiley Online Library for rules of use; OA articles are governed by the applicable Creative Commons License